WILEY | Hindawi

Research Article

Study on Energy Conversion Efficiency and Structure Optimization of the Multorifices Nozzle for Radial Jet Drilling

Famu Huang,[1] **Ziheng Zhu,**[1] **Jian Wang,**[1] **Ping Zhang,**[1] **Zhongxin Ren,**[1] **Jun Lu,**[1] **Haibo Su,**[1] **Hong Zhang,**[1] **and Jingbin Li** [iD][2]

[1]*PipeChina, Beijing 102249, China*
[2]*State Key Laboratory of Petroleum Resources and Prospecting, China University of Petroleum Beijing, Beijing 102249, China*

Correspondence should be addressed to Jingbin Li; lijb@cup.edu.cn

Underground gas storage (UGS) is a crucial method for mitigating seasonal fluctuations in natural gas consumption. However, in China, UGS is primarily achieved through the conversion of abandoned gas reservoirs with limited storage capacity. Radial jet drilling (RJD) is an effective technology for the secondary development of depleted reservoirs. The multiorifice nozzle is a critical component that can efficiently break rock and create radial holes to increase gas production. In this study, we investigate the impact of nozzle structure on energy conversion efficiency through numerical simulations and experiments. Additionally, we design a swirling multiorifice nozzle and verify its effectiveness in field applications. Our findings indicate that the nozzle pressure drop and vorticity are primarily generated at the acute angle of the orifices. The number of forward orifices is directly proportional to energy loss, while the discharge coefficient and hydraulic performance initially increase and then decrease. Swirling multiorifice nozzle have fewer backward orifices, so they have less energy loss and a larger discharge coefficient. It has achieved better rock-breaking results in field applications. In conclusion, this study provides theoretical guidance and technical support for the secondary development of gas storage.

1. Introduction

Natural gas plays a crucial role in the modern energy systems [1]. With the rapid development of the natural gas industry, the consumption of natural gas has been growing at a rate of nearly 10% per year, and ensuring a stable supply has become a major issue affecting living standards of people [2]. Underground gas storage is an important means of alleviating seasonal differences in natural gas consumption [3], and its profile schematic is shown in Figure 1. Most of the UGS facilities are concentrated in the United States, the European Union, and Russia. Their geological formations are simple, the burial depth is shallow, and the reservoirs belong to the high-porosity and high-permeability types [4]. The difficulty of development and construction is relatively small, and supporting technologies suitable for corresponding UGS facilities have been established [5]. At the end of the 20th century, China began to invest in the UGS facilities, and now turned into a period of rapid growth. In the past 20 years, 27 types of UGS facilities have been built, with a total working capacity of 1.64×10^{10} m³ [6, 7]. UGS facilities in China have the characteristics of deep burial, fractured structures, strong reservoir heterogeneity, high pressure, complex injection, and extraction systems [8, 9].

Radial jet drilling (RJD) can penetrate the near-well contamination zone, enhance the single-well control area, improve the distribution of reservoir pressure, significantly increase oil and gas recovery and single-well production, and minimize formation pollution, as illustrated in Figure 2 [10, 11]. It has become an effective method for the secondary growth of depleted petroleum and gas reservoirs [12–14]. RJD has been applied or tested in several countries, including the United States, Canada, China, and Russia [15–20].

The multiorifice nozzle is an efficient nozzle used in RJD applications [21–23], as shown in Figure 2. The forward orifice of the nozzle generates a forward-velocity jet that breaks the formation to create a radial borehole. The backward orifice produces a backward-velocity jet that creates reverse
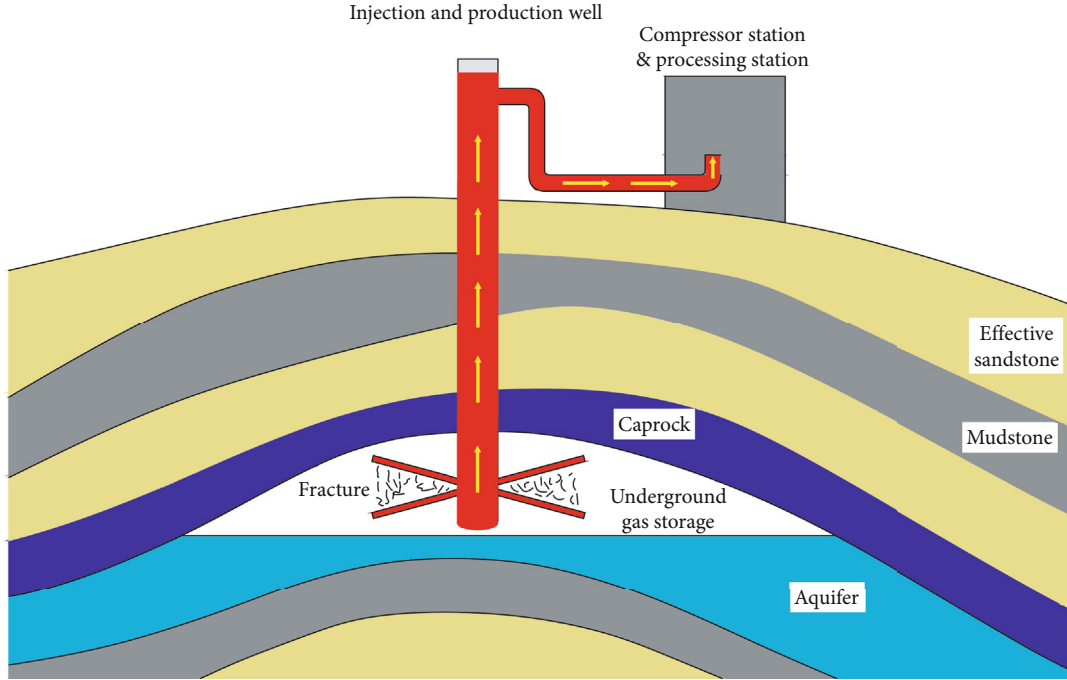
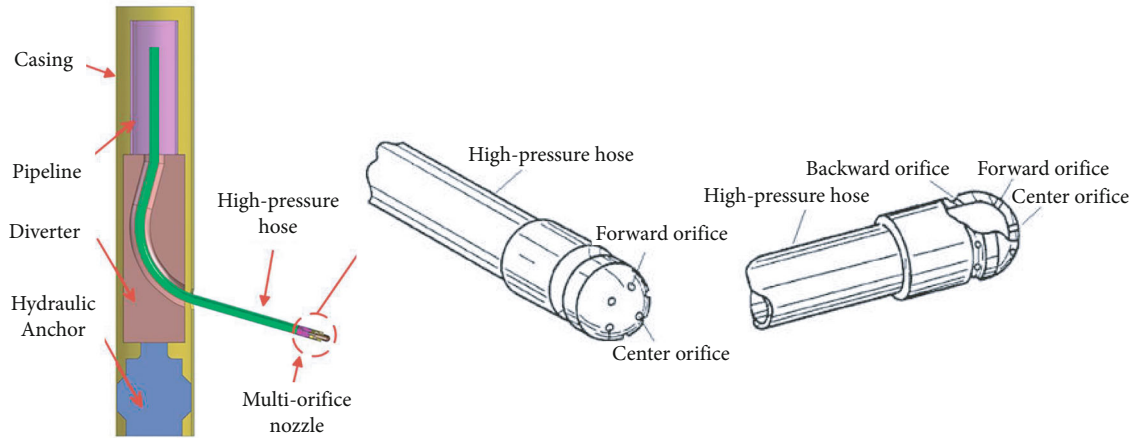FIGURE 1: Schematic diagram of underground gas storage.

FIGURE 2: Radial jet drilling (RJD) technology [12] and schematic of multiorifice nozzle.

thrust through interaction with the wellbore wall. The combined action of the two opposing jets propels the nozzle assembly further into the formation. Buset et al. [24] analyzed the mechanism of rock breaking and the self-propelled ability of the multiorifice nozzle. Liao et al. [25] conducted investigations into the impact of hydraulic parameters and the number of forward orifices on rock-breaking properties [26]. Meanwhile, Zhongwei et al. [27] explored the design of a swirling jet multiorifice nozzle for radial horizontal well technology, which found that a 30° inclination angle of the borehole was most effective for rock breaking. However, due to the low discharge coefficient of multiorifice nozzles, only a small amount of hydraulic energy is transferred to the fluid, limiting its conversion efficiency [28]. The present study is aimed at investigating how

nozzle structure affects energy conversion efficiency through numerical simulation and experiments, with a focus on designing and testing a swirling multiorifice nozzle for field applications.

2. Equation of the Nozzle Discharge Coefficient

From Bernoulli's theorem [29], the pressure drop can be calculated by

$$\Delta p = \frac{1}{2} \frac{\rho Q^2}{C^2 A^2} \times 10^{-6}, \tag{1}$$

where Δp is the pressure drop of the nozzle, MPa. ρ is density, kg/m^3. Q is the flow rate, m^3/s. A is the equivalent cross-
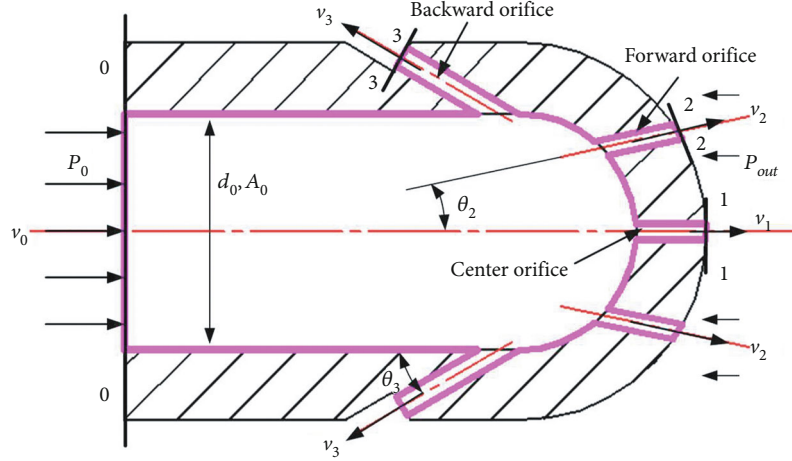
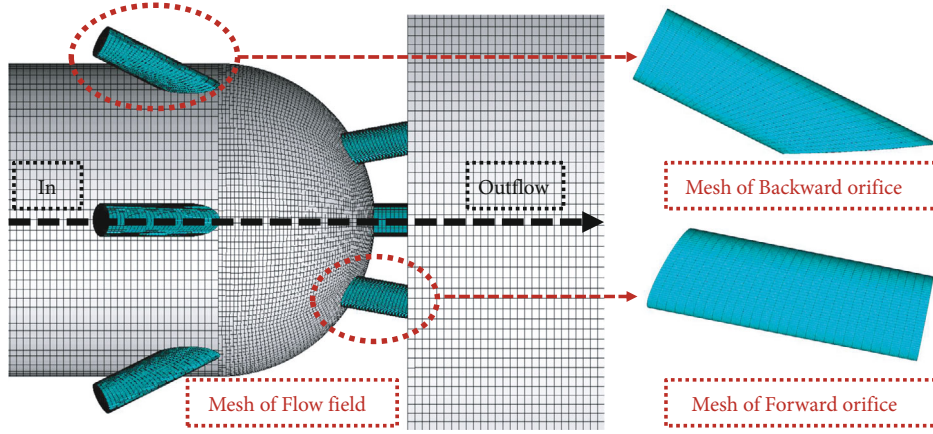FIGURE 3: Structural diagram of the multiorifice nozzle.

FIGURE 4: The flow field model of the multiorifice nozzle and mesh strategy.

sectional area, m^2. C is the discharge coefficient, dimensionless. The cross-section area can be expressed by

$$\frac{A_i}{A} = \frac{d_i^2}{d^2}.$$ (2)

A_i is the cross-sectional area of each orifice, m^2. d_i is the diameter of each orifice, m. d is the equivalent diameter, m.

Based on the relationship between pressure drop and flow rate for a cone nozzle, it can be inferred that there is a distinct quadratic association between these two parameters. Using the equation of continuity, the average velocity ($\bar{v}$, m/s) of the nozzle can be determined.

$$\bar{v} = \frac{Q}{A}.$$ (3)

By substituting Equation (2) into Equation (1), and separating the pressure section and velocity section, Equation (1) is found to be

$$\frac{1}{2}\rho\bar{v}^2 \times 10^{-6} = C^2 \Delta p.$$ (4)

TABLE 1: Conversion of flow rate and velocity.

Flow rate, L/s	0.772	0.722	0.672	0.622	0.572	0.522
Velocity, m/s	10.892	10.186	9.481	8.775	8.069	7.363

By substituting this expression into the pressure and velocity sections of the nozzle's energy equation, it can be observed that the nozzle discharge coefficient plays a critical role in determining the energy conversion efficiency of multiorifice nozzles [1]. Therefore, understanding the discharge coefficient is crucial for optimizing hydraulic energy utilization. This coefficient can be calculated as a function of water density, flow rate, jetting pressure, and equivalent outlet area, as described in Equation (1).

$$C = \frac{\sqrt{\rho Q^2 / (2 \Delta p A^2)}}{1000}.$$ (5)

3. Simulation and Experiment

3.1. Structure of the Nozzle. Figure 3 illustrates a multiorifice nozzle and its simplified physical model. The nozzle comprises a central orifice, n_2 forward orifices, and n_3 backward
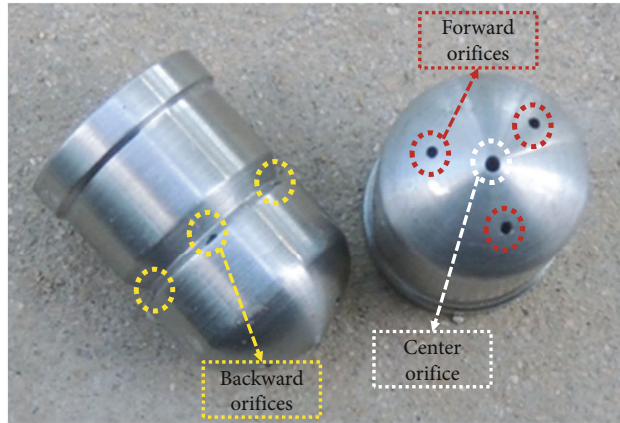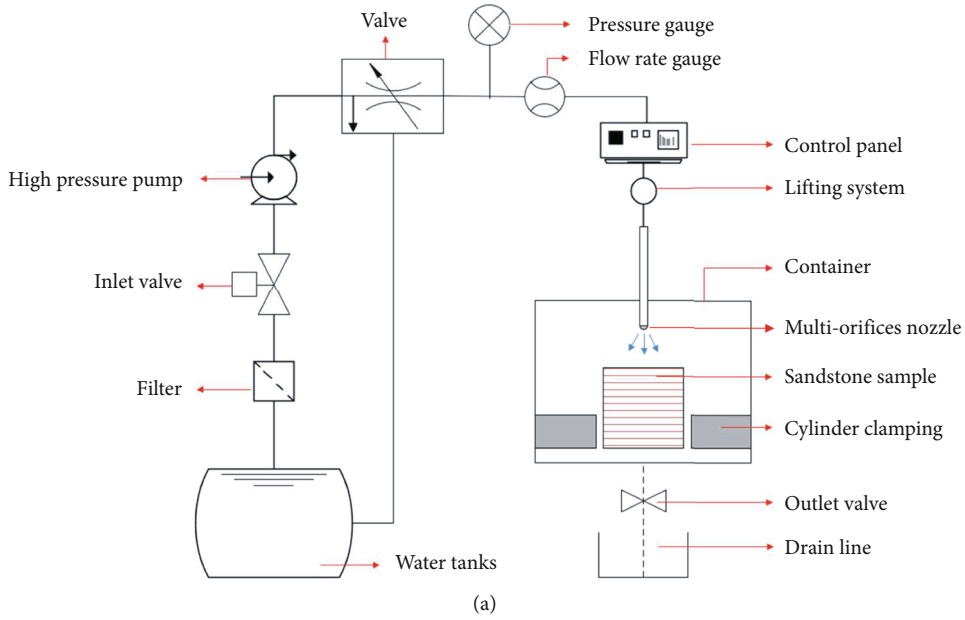
(a)

(b)

FIGURE 5: (a) Schematic diagram of the sandstone-breaking device. (b) Physical diagram of the multiorifice nozzle (6 + 3 + 1).

(a)

(b)
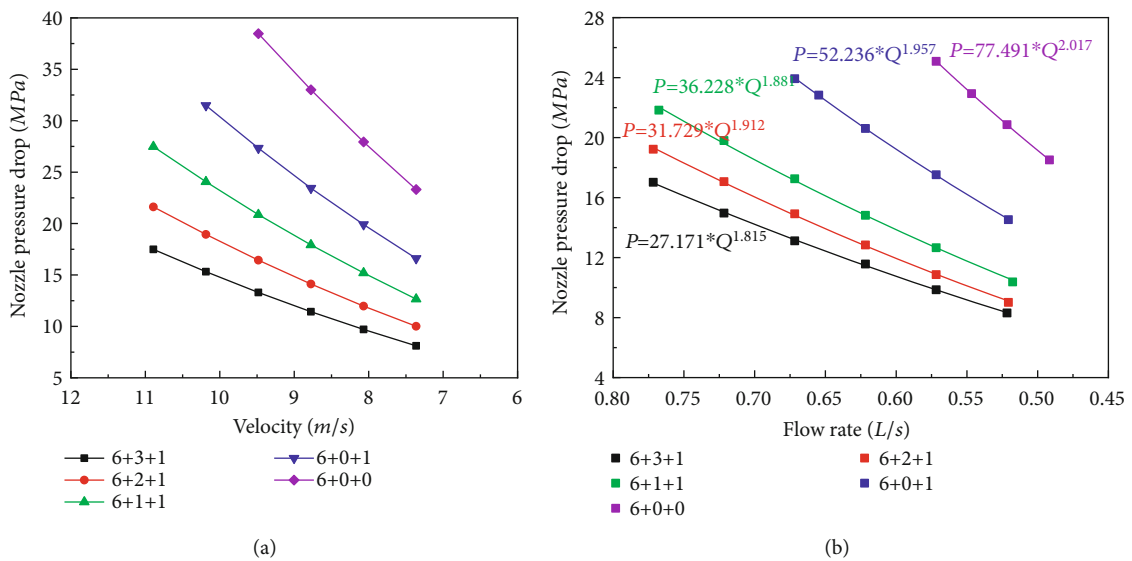
FIGURE 6: (a) Velocity–nozzle pressure drop curves in the simulation. (b) Flow rate-nozzle pressure drop curves in the experiment.
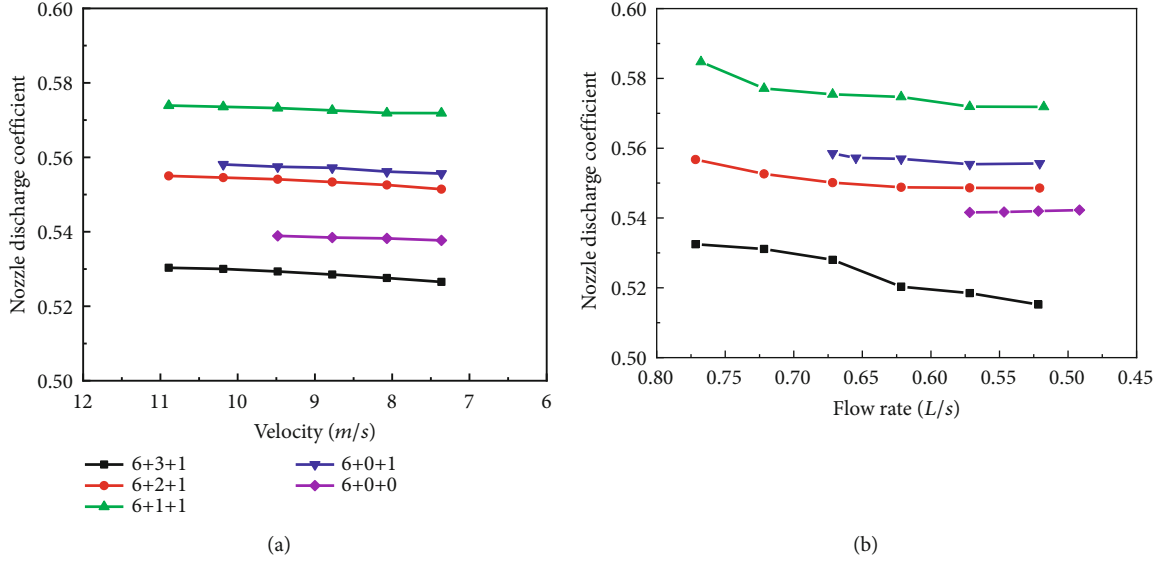
(a)

(b)

FIGURE 7: (a) Velocity-nozzle discharge coefficient curves of different nozzles in the simulation. (b) Flow rate-nozzle discharge coefficient curves of different nozzles in the experiment.
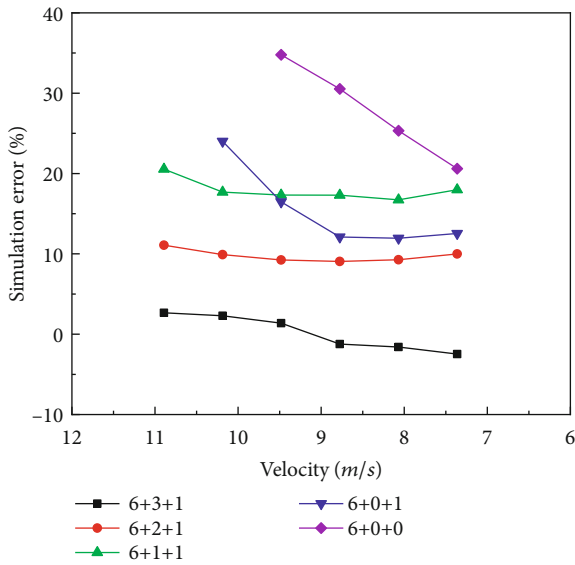

FIGURE 8: Simulation errors in the simulation and experiment.

FIGURE 9: Curve of nozzle discharge coefficient-number of forward and central orifices.

orifices; hence, it is classified as $n_3 + n_2 + 1$ type. The orifices have diameters of d_1, d_2, and d_3, velocities of v_1, v_2, and v_3, and flow rates of Q_1, Q_2, and Q_3. The angles between the center axis of the forward and backward orifices are denoted as θ_2 and θ_3. The diameter of the nozzle is d_0. The incoming fluid is characterized by its velocity, flow rate, and pressure, which are represented by v_0, Q_0, and P_0, respectively. The diameter of the nozzle inlet is d_0. The outlet pressure of the orifices is denoted as p_{out}.

3.2. Simulation and Experiment Scheme.

In this study, the flow fields of the multiorifice nozzle were numerically simulated using Ansys Fluent [30]. The flow field model of the $6 + 3 + 1$ nozzle and its mesh strategy are presented in Figure 4. The models were discretized using an O-type
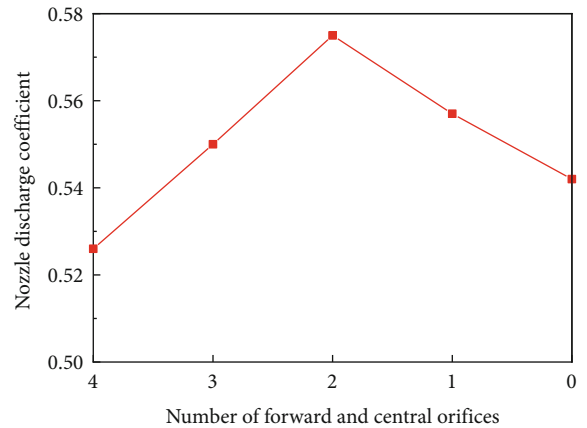
scheme with the ICEM code, and the grids were structured hexahedral cells [31]. Notably, the mesh was refined in the region of accelerated fluid flow to enhance computational accuracy. Additionally, the mesh of the hemispherical structure connected with the forward orifices was also refined.

The inlet of the multiorifice nozzle was set as the velocity inlet, and the inlet velocity value was calculated using the corresponding flow rate in Equation (2), as presented in Table 1. The backward orifices, forward orifices, and central orifice were set as pressure outlets, with the value being atmospheric pressure. The wall of the multiorifice nozzle was set as the nonslip wall. In this study, the submerged jet was turbulent in the vapor-liquid two-phase flow field [32]. Therefore, the numerical simulation employed the multiphase and turbulence models, with the governing equations found in reference [33].

The schematic diagram of the sandstone-breaking device and the physical diagram of the multiorifice nozzle are
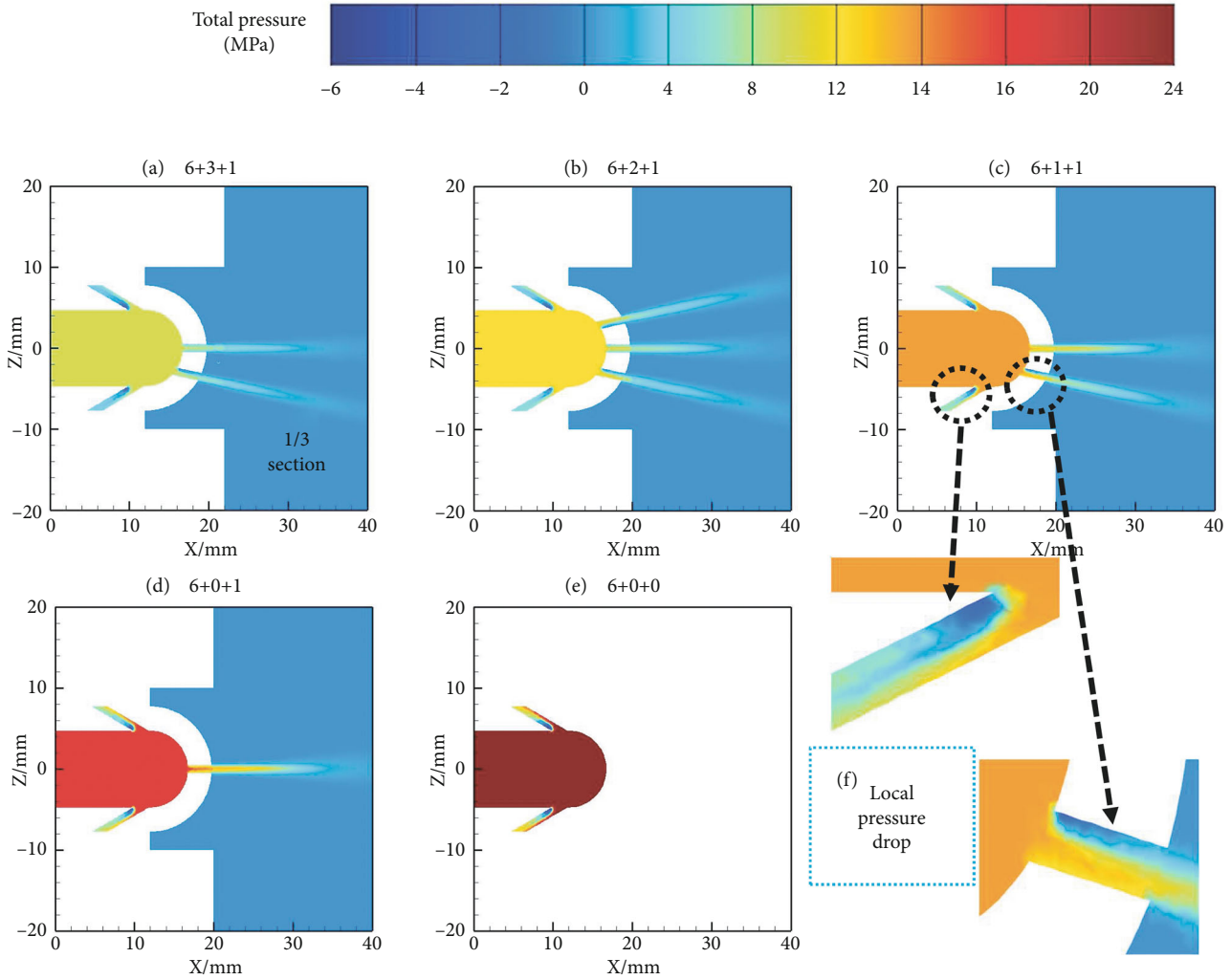
Figure 10: The total pressure distribution of different nozzles when the flow rate is 0.522 L/s.

illustrated in Figure 5. By measuring the inlet velocity and pressure drop during rock breaking, the discharge coefficient was calculated based on Equation (4).

3.3. Comparison of Simulation and Experimental. Figure 6 illustrates velocity–nozzle pressure drop curves in the simulation and flow rate-nozzle pressure drop curves in the experimental results. The results indicate that the numerical simulation of nozzle pressure drop follows a quadratic relationship. It is consistent with the experimental findings. The pressure drop increases with an increase in velocity, and a decrease in the number of forward orifices leads to a reduction in the equivalent diameter, resulting in an increase in the nozzle pressure drop. Consequently, nozzles with fewer forward orifices have a smaller equivalent diameter and a lower allowable flow rate. To ensure safety, only the first four groups of flow rates were considered in both the simulation and experimental studies.

Figure 7 illustrates velocity–nozzle discharge coefficient curves in the simulation and flow rate-nozzle discharge coefficient curves in the experimental results. The discharge coefficient can be calculated using Equation (4) and the pres-sure drop data from Figure 6. The results indicate that all discharge coefficients are less than 0.6, and they remain relatively constant with an increase in flow rate. The discharge coefficient initially increases and then decreases with a decrease in the number of preholes, with the $6 + 1 + 1$ nozzle having the highest discharge coefficient. These findings demonstrate that modifying the nozzle structure can significantly enhance hydraulic performance, while flow rate has a minimal impact on hydraulic performance.

Figure 8 illustrates that the numerical simulation of the discharge coefficient yields higher values than the experimental results at the same flow rate. Moreover, the discrepancy increases with the rise in flow rate and the reduction in the number of forward orifices. This can be attributed to the neglect of the cavitation effect and viscous resistance in the numerical model. As the flow rate increases, the fluid velocity also increases, leading to a stronger cavitation effect and higher viscous resistance in the high-velocity fluid. Consequently, the error increases with the rise in flow rate and the decrease in the number of forward orifices. Notably, when the flow rate is below 0.672 L/s, the error of the $6 + 1 + 1$ nozzle is greater than
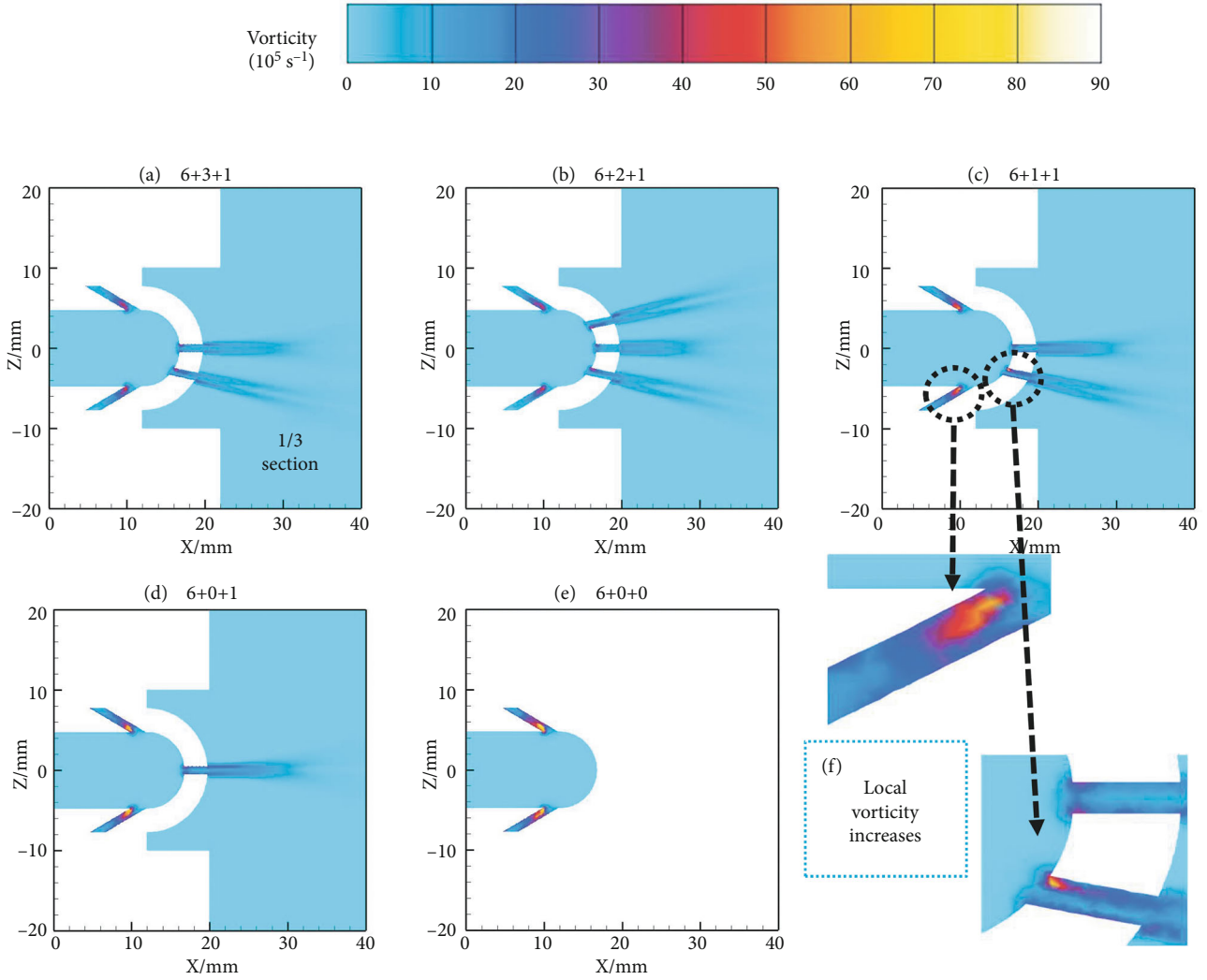
FIGURE 11: The vorticity distribution of different nozzles when the flow rate is 0.522 L/s.

that of the $6 + 1 + 1 + 1$ nozzle. This suggests that the cavitation effect and viscous resistance of the $6 + 1 + 1$ nozzle are more pronounced at a specific flow rate, and its fluid velocity is higher. This finding is consistent with the maximum discharge coefficient of the $6 + 1 + 1$ nozzle observed in the experimental analysis.

3.4. Optimization of Forward Orifice Number. In general, the discharge coefficient is expected to increase with the number of forward orifices. However, this assumption needs to be validated by numerical simulations and experimental results. Since the flow rate has a negligible effect on the discharge coefficient, the relationship between the number of forward orifices and the discharge coefficient was plotted at a flow rate of 0.522 L/s. As depicted in Figure 9, the discharge coefficient initially increases and then decreases, reaching its maximum value when the number of forward orifices is 2. This trend may be attributed to the increased complexity of the flow structure when the number of forward orifices is 3 or 4, leading to greater local energy losses.

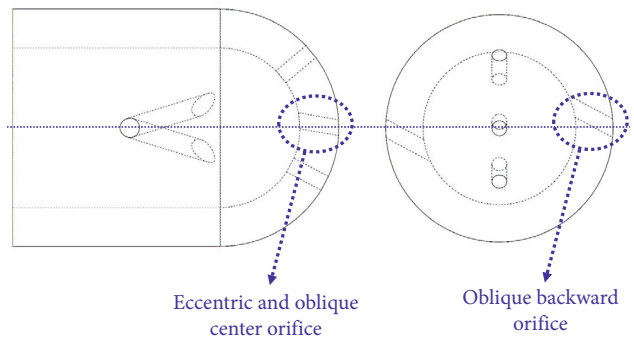FIGURE 12: Structure of the swirling multiorifice nozzle. (a) Transverse profile. (b) Top perspective view.

3.5. Distribution of Total Pressure and Vorticity. By conducting numerical simulations to calculate the pressure and vorticity distributions of the flow field in a multiorifice nozzle, the pressure loss of the flow field can be visually observed. The relationship between the nozzle discharge
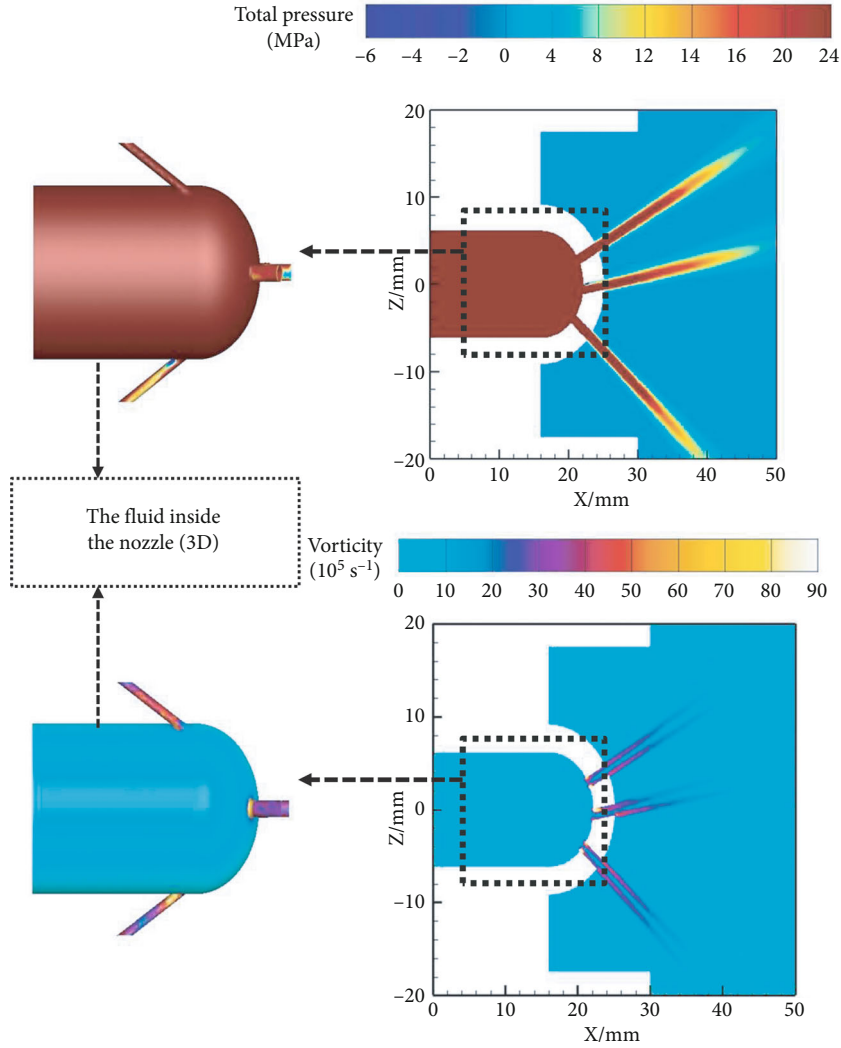
FIGURE 13: The total pressure and vorticity distribution of swirling multiorifice nozzle when the flow rate is 0.522 L/s.

coefficient/inlet velocity and number of forward orifices can be explained.

Figure 10 shows the total pressure distribution of different nozzles at a flow rate of 0.522 L/s. For the 6 + 3 + 1 nozzle, the three outlets of the forward orifices are evenly distributed around the z-axis, and one of the planes is selected for analysis. As depicted in Figures 10(a)–10(e), the total pressure of the jet flow field inside the nozzles increases as the number of forward orifices decreases, indicating a negative correlation. Figure 10(f) reveals a local negative pressure in the critical steering part of the backward and forward orifices, indicating a significant pressure loss in this region. Since the number of backward orifices is fixed at 6 in both the experimental and numerical simulation schemes, it can be inferred that the greater the number of forward orifices, the higher the local pressure loss. This finding is consistent with the experimental results that the number of forward orifices affects the discharge coefficient.

Vorticity is a fundamental physical quantity used to describe the intensity and direction of fluid flow, representing the rotation of the fluid velocity vector. A higher vortic-
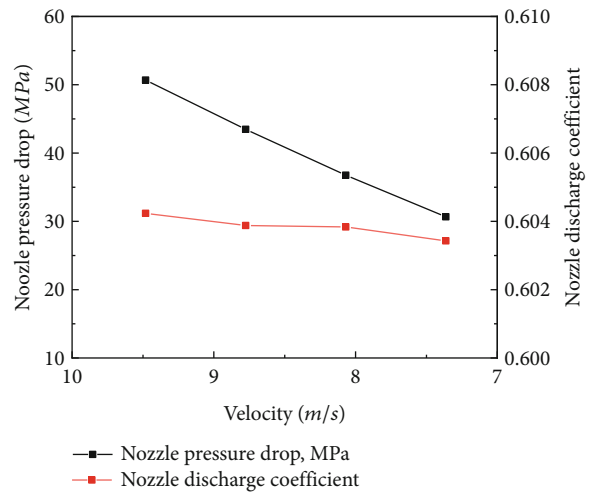

FIGURE 14: The velocity-pressure drop–discharge coefficient curve of the swirling multiorifice nozzle.
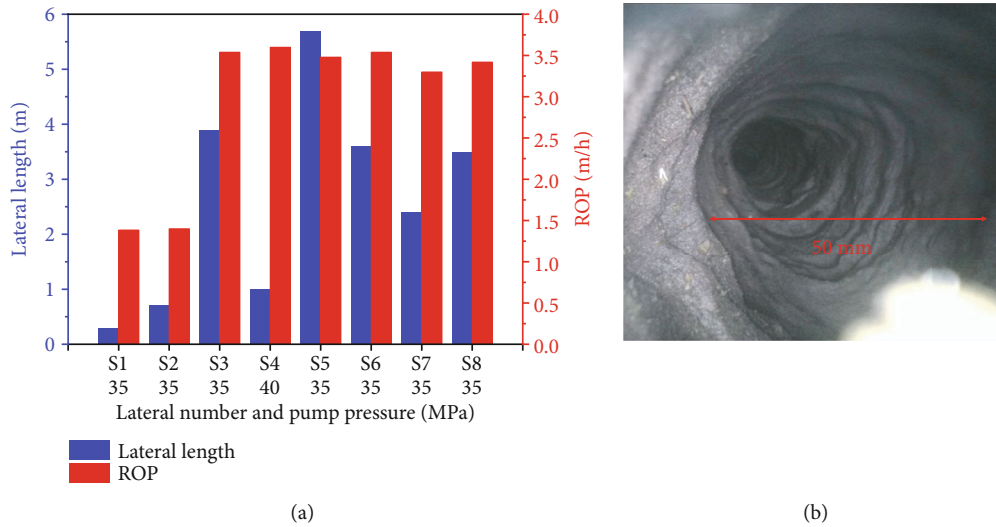
(a)

(b)

FIGURE 15: (a) The length and ROP of different laterals. (b) Endoscopic figure of the lateral S8 [28].

ity indicates a greater swirl intensity and a more intricate flow field structure [34].

Figure 11 displays the vorticity distribution of different nozzles at a flow rate of 0.522 L/s, with one of the planes selected for analysis in the 6 + 3 + 1 nozzle. As shown in Figure 11(f), the vorticity in the critical steering part of the backward and forward orifices becomes more concentrated, indicating a more complex flow field structure in this region. However, this phenomenon is not observed in the forward center nozzle. As depicted in Figures 11(a)–11(e), the vorticity increases as the forward orifices decrease. Since the backward orifices is fixed at 6 in the scheme design, it can be inferred that a greater number of forward orifices generates higher vorticity and a more intricate flow field structure inside the nozzle. This finding is consistent with the experimental results that the number of forward orifices affects the nozzle discharge coefficient.

4. Numerical Simulation of the Swirling Multiorifice Nozzle

4.1. Structure of the Swirling Multiorifice Nozzle. Through numerical simulation and experimental study of a multiorifice nozzle, it has been observed that the energy loss is more significant at the acute angle of the backward orifice. To address this issue, a swirling multiorifice nozzle has been designed, as depicted in Figure 12. The backward orifice of the swirling multiorifice nozzle is set as an oblique orifice with a count of 2. It aims to achieve the hole forming-effect of the multiorifice nozzle, reduce energy loss, and enhance rock-breaking efficiency. To ensure high efficiency of the swirling multiorifice nozzle and to achieve roundness and smoothness of the hole, the center orifice is designed to be eccentric and oblique [26].

4.2. Distribution of Total Pressure and Vorticity. Figure 13 illustrates the total pressure and vorticity distribution of the swirling multiorifice nozzle at a flow rate of 0.522 L/s. As the backward orifice of the swirling multiorifice nozzle

is eccentric and not in the same section as the forward orifice, the forward orifice profile and the 3D fluid model inside the nozzle are selected for analysis. The results in Figure 13 indicate that the sharp-angle steering parts of the three forward orifices of the swirling multiorifice nozzle all produce significant pressure drops and vorticity. Additionally, the backward orifices of a swirling multiorifice nozzle have smaller acute angles. Although the pressure drop and vorticity of a single backward orifice are large, the backward orifices are small. Therefore, further analysis is required to determine the discharge coefficient and energy conversion efficiency.

4.3. Optimization of the Swirling Multiorifice Nozzle. To ensure safe pressure, numerical simulation of the swirling multiorifice nozzle was conducted only under a small flow rate. Figure 14 presents the velocity-nozzle pressure drop-nozzle discharge coefficient curve obtained from numerical simulation. As the flow rate increases, the nozzle pressure drop gradually increases, and the pressure value at high flow rates exceeds the safe pressure limit of 40 MPa. The discharge coefficient remains relatively stable, with a slight increase observed. However, all discharge coefficients are greater than 0.6, indicating a significant improvement in hydraulic performance.

5. Field Application of the Swirling Multiorifice Nozzle

Based on the experimental test results [28], it was verified through field application that eight well stages were drilled. The velocity and depth of drilling in the field were controlled and recorded by an auxiliary traction device, with an initial drilling speed of 1.8 m/h. During the drilling process, the match between the feeding speed and the pore formation speed was determined based on the force state of the swirling multiorifice nozzle, and the maximum pore formation speed was obtained. The length and rate of penetration (ROP) of the eight well laterals were obtained, as shown in Figure 15(a). When

using unoptimized multiorifice nozzles during drilling in well 1 and well 2, the drill tool encountered strong resistance and could not penetrate the formation after drilling a short distance. However, with the optimized swirling multiorifice nozzle, the average ROP increased from 1.4 m/h to 3.6 m/h, and the average lateral length increased from 0.5 m to 3.35 m. These results demonstrate that the optimized swirling multiorifice nozzle can significantly improve the drilling rate and hole length of the RJD system. The maximum ROP achieved was 3.6 m/h, and the maximum radial lateral length was 5.7 m, confirming the reliability of the developed radial jet drilling (RJD) system.

In the eighth well section, the cliff was successfully penetrated, and an endoscope was used to capture images of the lateral wellbore's internal morphology. The results revealed a smooth, round profile with some local irregularities, as shown in Figure 15(b). The lateral has an average diameter of approximately 50 mm (1.94 in), which is more than twice the maximum outer diameter of the nozzle, indicating high rock-breaking efficiency. During the drilling process, each jet created rock-breaking pits along a spiral path that overlapped with one another, resulting in a regular lateral profile. The ring-shaped bulge observed along the path is attributed to fluid erosion.

6. Conclusions

The hydraulic performance of multiorifice nozzles is severely limited by their energy conversion efficiency, which is determined by the discharge coefficient. To investigate the influence of velocity and nozzle structure on the discharge coefficient, experiments and numerical simulations were conducted. Based on these findings, a swirling multiorifice nozzle was designed. The following conclusions were drawn:

(1) The primary energy loss in multiorifice nozzles is due to the acute angle of the orifices, which decreases slightly with increasing velocity but increases significantly with the number of orifices

(2) The energy loss, discharge coefficient, and hydraulic performance increase initially and then decrease as the forward orifices increases

(3) Swirling multiorifice nozzle have fewer backward orifices, so they have less energy loss and a larger discharge coefficient. It has achieved better rock-breaking results in field applications

Nomenclature

A:　Equivalent cross-sectional area, m^2
A_i:　Cross-sectional area of each orifice, m^2
C:　Nozzle discharge coefficient, dimensionless
d:　Equivalent diameter, m
d_0:　Diameter of the nozzle inlet, m
d_i:　Diameter of each orifice, m
D:　Diameter of the larger pipe, m
g:　Gravitational acceleration, m/s^2
L_i:　Length of the orifice, mm
v_0:　Velocity of the inlet water liquid, m/s
$\bar{v}$:　Average velocity of the water liquid, m/s
P_0:　Pressure of the inlet, MPa
P_{out}:　Outlet pressure, or the submerge pressure, MPa
$\triangle p$:　Pressure drop of the nozzle, MPa
Q_0:　Flow rate of the nozzle inlet, L/s
ρ:　Density of water liquid, kg/m^3
θ_i:　Angles between the center axis of the orifices and the nozzle ($i = 2, 3$).

Data Availability

The data that support the findings of this study are available in "Field test of radial jet drilling technology in a surface formation" at doi:10.1016/j.petrol.2022.110928 [28], and "The self-propelled force model of a multiorifice nozzle for radial jet drilling" at doi:10.1016/j.jngse.2015.04.009 [26]. When data is required, the corresponding author can be contacted.

Conflicts of Interest

The authors declare no conflict of interest.

Authors' Contributions

Conceptualization was worked on by Famu Huang and Ziheng Zhu. The methodology was performed by Famu Huang and Ping Zhang. The equation was done by Famu Huang and Jian Wang. The experiment was conducted by Famu Huang, Zhongxin Ren, Jun Lu, and Haibo Su. Software was worked on by Jingbin Li and Hong Zhang. The validation was done Famu Huang and Ziheng Zhu. Formal analysis was conducted by Famu Huang. The investigation was performed by Ping Zhang. Resources was supervised by Jian Wang. The data curation was charged to Ziheng Zhu. Writing—original draft preparation was done by Famu Huang. Writing—review and editing—was worked on by Ping Zhang. Visualization was managed by Hong Zhang. All authors have read and agreed to the published version of the manuscript.

Acknowledgments

References

[1] B. Lin and S. Agyeman, "Impact of natural gas consumption on sub-Saharan Africa's CO$_2$ emissions: evidence and policy perspective," *Science of The Total Environment*, vol. 760, no. 1, article 143321, 2021.

[2] J. Li, Y. She, Y. Gao, M. Li, G. Yang, and Y. Shi, "Natural gas industry in China: development situation and prospect," *Natural Gas Industry*, vol. 7, no. 6, pp. 604–613, 2020.

[3] L. Jianwen, J. Wang, and W. Haifeng, "Analysis on the cause and influence of natural gas peak-valley gap of Beijing-Tianjin-Hebei region," *International Petroleum Economics*, vol. 28, no. 12, pp. 45–53, 2020.

[4] X. Shi, W. Liu, J. Chen et al., "Softening model for failure analysis of insoluble interlayers during salt cavern leaching for natural gas storage," *Acta Geotechnica*, vol. 13, no. 4, pp. 801–816, 2018.

[5] L. Jianxun and L. Yan, "Development status and prospects of China's underground gas storage construction," *Applied Chemical Industry*, vol. 51, no. 4, pp. 1136–1140, 2022.

[6] Z. Jindong, *Theory and Simulation Research of Seepage in Low Permeability Underground Natural Gas Storage*, Harbin Institute of Technology, 2021.

[7] National Energy Administration and Development Research Center of the State Council, "China natural gas development report -2021," *Petroleum Industry Press*, vol. 202, pp. 1–9, 2021.

[8] Z. Qingfu, W. Jie, and X. Bo, "Enlightenment of underground gas storage management system in Europe and the US to China," *Logistics Technology*, vol. 34, no. 6, pp. 94–97, 2015.

[9] J. Zhang, Y. Tan, T. Zhang, K. Yu, X. Wang, and Q. Zhao, "Natural gas market and underground gas storage development in China," *Journal of Energy Storage*, vol. 29, article 101338, 2020.

[10] W. Dickinson and R. W. Dickinson, "Horizontal radial drilling system," in *SPE California Regional Meeting*, Bakersfield, CA, USA, 1985.

[11] W. Dickinson, R. R. Anderson, and R. W. Dickinson, "The ultrashort-radius radial system," *SPE Drilling Engineering*, vol. 403, pp. 247–254, 1989.

[12] C. Yunxing, S. Fen, and T. Lin, "Development and application of dense multi-cluster fracturing in horizontal wells for low permeability and low pressure coal reservoir," *Journal of China Coal Society*, vol. 45, no. 10, pp. 3512–3521, 2020.

[13] Y. Jianping, Y. Zhaozhong, and X. Rigui, "Synchronous hydraulic conformance fracturing technology used for deep coal beds and its field application in the southern Qinshui Basin," *Natural Gas Industry*, vol. 37, no. 10, pp. 35–45, 2017.

[14] W. Hai, Y. Zhaozhong, and L. Yue, "Study on drilling and fracturing technology for deep complex structure coal reservoir in Qin Shui Basin," *Coal Science and Technology*, vol. 47, no. 9, pp. 105–111, 2019.

[15] G. Boyun, S. Rashid, and Y. Xu, "Analytical model for predicting productivity of radial-lateral wells," *Energies*, vol. 13, no. 23, p. 6386, 2020.

[16] W. D. Gunter, T. Gentzis, B. A. Rottenfusser, and R. J. H. Richardson, "Deep coalbed methane in Alberta, Canada: a fuel resource with the potential of zero greenhouse gas emissions," *Energy Conversion and Management*, vol. 38, pp. 217–222, 1997.

[17] M. J. Kotarba, "Composition and origin of coalbed gases in the Upper Silesian and Lublin basins, Poland," *Organic Geochemistry*, vol. 32, no. 1, pp. 163–180, 2001.

[18] K. S. Narasimhan, A. K. Mukherjee, S. Sengupta, S. M. Singh, and M. M. Alam, "Coal bed methane potential in India," *Fuel*, vol. 77, no. 15, pp. 1865-1866, 1998.

[19] S. C. Huang, W. G. Liu, and G. Q. Zhao, "Coalbed methane development and utilization in China: status and future development," *China Coal*, vol. 35, 2009.

[20] S. Krivoshchekov, A. Kochnev, and E. Ozhgibesov, "The application of neural networks to forecast radial jet drilling effectiveness," *Energies*, vol. 15, no. 5, p. 1917, 2022.

[21] L. Jingbin, H. Zhongwei, Z. Guangqing, L. Xin, and L. Huan, "Rock breaking characteristics of the self-rotating multi-orifices nozzle applied to coalbed methane radial jet drilling," *International Journal of Rock Mechanics and Mining Sciences*, vol. 136, article 104483, 2020.

[22] Z. Tao, L. Yumei, L. Hui, and J. Jianing, "Simulation and experimental study on characteristics of multiorifice nozzle in radial jet drilling," *Geofluids*, vol. 2022, Article ID 2531181, 8 pages, 2022.

[23] W. L. Carl, "Method of and apparatus for horizontal well drilling," US Patent 5-853056, 1993.

[24] P. Buset, M. Riiber, and A. Eek, "Jet drilling tool: cost-effective lateral drilling technology for enhanced oil recovery," in *All Days*, Houston, TX, USA, 2001.

[25] H. Liao, J. Niu, Y. Cheng, Z. Huang, and D. Ma, "Experiment study on water jet breaking rock by multi-orifice nozzle," *Journal of China Coal Society*, vol. 36, pp. 1858–1862, 2011.

[26] J. Li, G. Li, Z. Huang, X. Song, R. Yang, and K. Peng, "The self-propelled force model of a multi-orifice nozzle for radial jet drilling," *Journal of Natural Gas Science and Engineering*, vol. 24, pp. 441–448, 2015.

[27] H. Zhongwei, L. Zhijun, L. Gensheng et al., "Oriented and sand control hydra-jet fracturing in coalbed methane horizontal wells and field applications," *Journal of China Coal Society*, vol. 47, no. 7, pp. 2687–2697, 2022.

[28] L. Jingbin, H. Zhe, L. Gensheng, H. Zhongwei, D. Jiacheng, and C. Kang, "Field test of radial jet drilling technology in a surface formation," *Journal of Petroleum Science and Engineering*, vol. 218, 2022.

[29] J. H. Hogh, "Flow measurements with orifices and nozzles at the low Reynolds numbers encountered in process pilot plants," in *The 7th World Petroleum Congress*, Mexico City, Mexico, 1967.

[30] Z. Dongqing, L. Jingbin, H. Xiao, L. Xin, and C. Kang, "Flow field simulation of swirling abrasive jet nozzle for hard rock breaking," *Geofluids*, vol. 2022, Article ID 4681189, 13 pages, 2022.

[31] Z. Li, D. Zheng, F. Hong, and D. Ni, "Numerical simulation of the sheet/cloud cavitation around a two-dimensional hydrofoil using a modified URANS approach," *Journal of Mechanical Science and Technology*, vol. 31, no. 1, pp. 215–224, 2017.

[32] Y. Chen, J. Li, Z. Gong, X. Chen, and C. Lu, "Large Eddy simulation and investigation on the laminar-turbulent transition and turbulence-cavitation interaction in the cavitating flow around hydrofoil," *International Journal of Multiphase Flow*, vol. 112, pp. 300–322, 2019.

[33] Z. Yiqun, W. Xiaoya, Z. Shuai et al., "Numerical simulation of the straight-swirling integrated jet and its application in natural gas hydrate drilling," *SPE Journal*, vol. 27, no. 6, pp. 3724–3739, 2022.

[34] M. Girfoglio, A. Quaini, and G. Rozza, "A POD-Galerkin reduced order model for the Navier-Stokes equations in stream function-vorticity formulation," *Computers and Fluids*, vol. 244, article 105536, 2022.